Numerical and experimental modeling for thermal developing pipe flow with microwave heating

G. Cuccurullo, L. Giordano, and G. Viccione

***Abstract*—** The work here presented is concerned with the analysis of forced convection of Newtonian liquids flowing in a circular duct under microwave heating. Spatial temperature field in the illuminated cavity was numerically obtained by solving coupled energy and Maxwell's equations since it was assumed to be dependent on the dielectric properties of the fluid flowing in the duct. Attained temperature levels justified no phase changes and no gas phases. Temperature contour is detected by an outer infrared camera looking inside the microwave chamber in correspondence of the applicator-pipe. The proposed procedure is intended to realize relatively high spatial resolution temperature readings while microwave heating takes place. In facts, temperatures are usually measured in few points which can't enable a proper temperature profile reconstruction, the latter being strongly uneven along the pipe due to electromagnetic field distribution. Numerical results are compared with the corresponding experimental ones for different temperature levels, showing a good agreement.

***Keywords*—** CFD**,** Comsol multiphysics, FEM, Experimental validation, Fiberoptic probes, Infrared thermography, Infrared image processing, Maxwell's equations, Microwave heating of liquids, Newtonian liquids, Numerical modeling.

I. Introduction

MICROWAVE heating has been used predominantly as a batch processing and sporadically as a continuous process. In conventional heating (CH) warming is due to hot air convection whereas in microwaves heating (MH) it takes place directly inside the exposed mass [1, 2]. MH techniques allow reduced time periods for processing, higher energy efficiency, absence of contaminants released in the environment. Despite of what above observed, some critical points should be addressed. Heating processing has been proved not to be uniform [3,4]. The magnitude and uniformity of electromagnetic energy absorption are affected by dielectric properties, ionic compounds, size and shape of the sample subjected to MW [5,6]. Such a problem is particularly evident in food industry. Different ingredients often have varying rates of energy absorption. In other terms, parts containing higher amounts of water tend to absorb microwave energy with a higher efficiency, while other parts with lower water content absorb heat more slowly, causing uneven heating. The reason is at molecular scale: electric dipoles of water molecule switch back and forth in the presence of the oscillating electromagnetic field. The overall efficiency of such a turning motion is enhanced when water is in the liquid state, due to the fact that liquid molecules move more freely than the molecules in the solid state, causing a major number of collisions and therefore more heat.

The inability of scaling-up and predicting temperature patterns leads to difficulties in practical plant design. Even more complications are involved wishing to consider continuous flow in MW heating: a numerical approach is mandatory, since energy, momentum and Maxwell equations are strongly coupled due to the need to consider dielectric properties temperature dependence [7]. Therefore, numerical modelling seems to be the only viable approach for reproducing such kinds of processes [8]. ANSYS Multiphysics [9] and COMSOL Multiphysics [7], [10-12] are among the most used commercial FEM codes for such a purpose. A comparison between ANSYS and COMSOL models is proposed in [13].

Several studies have been carried so far, as attempt to deal with the numerical modelling of MH of lossy substances, either in the liquid or solid state. Simple cases [14-16] started to be solved over the mid-1980s. Two- dimensional approaches were then proposed by [17-18]. In [17] the problem at hand is solved by a 2D finite element algorithm while in [18] effects of natural convection and dielectric properties were investigated. A number of three-dimensional algorithms have been proposed over the last few decades. It is worth mentioning the works by [19-20].

As a general rule, the correctness of the adopted numerical scheme should be checked by experimental validation of the results. This procedure is seldom adopted due to difficulties in reading out temperatures inside the illuminated cavity and therefore in controlling the magnetron delivered power. These issues can be surely included among the major hurdles in MW heating [19, 21]. In facts, heating control is realized measuring: 1) inlet and outlet temperatures of coils outside the MW cavity or 2) reading out temperatures in few points inside

G. Cuccurullo is with the Department of Industrial Engineering, University of Salerno, 84084 Fisciano ITALY, (corresponding author. Phone: +39 089-96-4444; e-mail: cuccuru@unisa.it).

L. Giordano is with the Department of Industrial Engineering, University of Salerno, 84084 Fisciano ITALY, (e-mail: lagiordano@unisa.it).

G. Viccione is with the Department of Civil Engineering, University of Salerno, 84084 Fisciano ITALY, (e-mail: gviccion@unisa.it).

the cavity by means of fiber optic probes. Unfortunately, as a consequence of the highly uneven electromagnetic field, irregular thermal patterns can be predicted: whishing numerical validation, an adequate number of sampling points is usually required to obtain reliable results. Advanced temperature mapping procedure using a 3D thermometry instrument, on the principles of Planar Laser Induced Fluorescence (PLIF) imaging, was proposed in [22]. On a wider scale, in [23] a microwave remote sensing procedure was proposed to detect the sea surface temperature.

To tackle with the issue related to the remote detecting of temperature patterns, the present paper aims to propose an attempt for realizing higher measurement resolutions based on quantitative infrared thermography temperature readout. The development of a proper procedure and a suitable data reduction are proposed to perform on line temperature readout inside the illuminated MW cavity.

The applicator-pipe is fed by continuous water flow and its wall temperatures are detected along the longitudinal axis; meanwhile, a corresponding numerical investigation was realized.

The water flow is supposed to be laminar hydrodynamically fully developed. Consider that laminar motion is not a limiting factor in MW heating since heat transfer is not driven by the wall to fluid temperature difference. However, it is often required due to the contemporary needs of realizing high temperature increases with relatively low power density. The high frequency electromagnetic field due to the 2450 MHz microwave unit in use and the subsequent thermal field were calculated by COMSOL Multiphysics. Water dielectric properties were assumed temperature dependent. The corresponding experimental tests encompassed two different inlet temperatures. Then, theoretical and experimental evidences were compared.

II. Proposed Methodology

A. *Experimental setup*

Experiments were performed in the available microwave pilot plant, Fig. 1. The oven was supported by a magnetron rated at 2 kW nominal power output and operating at a frequency of 2.45 GHz. The magnetron was connected to the cavity by a rectangular WR340 waveguide. The illuminated chamber was a cube 0.9 m side length. It housed the pyrex glass applicator-pipe (8 mm inner diameter, 1.5 mm thick) shipping water to be heated. The diameter choice is compliant with the electromagnetic skin depth; anyway, for the range of mass flow rates compatible with laminar motion, the design of pipe diameter was promptly done by employing the approach proposed by [24]. The inner chamber walls were insulated by polystyrene slabs black painted while the pipe longitudinal axis lied in a symmetry plane, thus suitably reducing the corresponding computational efforts. A variable-frequency drive was used to fine adjust pumping power supply to circulate water continuously feeding the applicator-pipe. Water was caught by a thermostatic bath enabling to fix its inlet

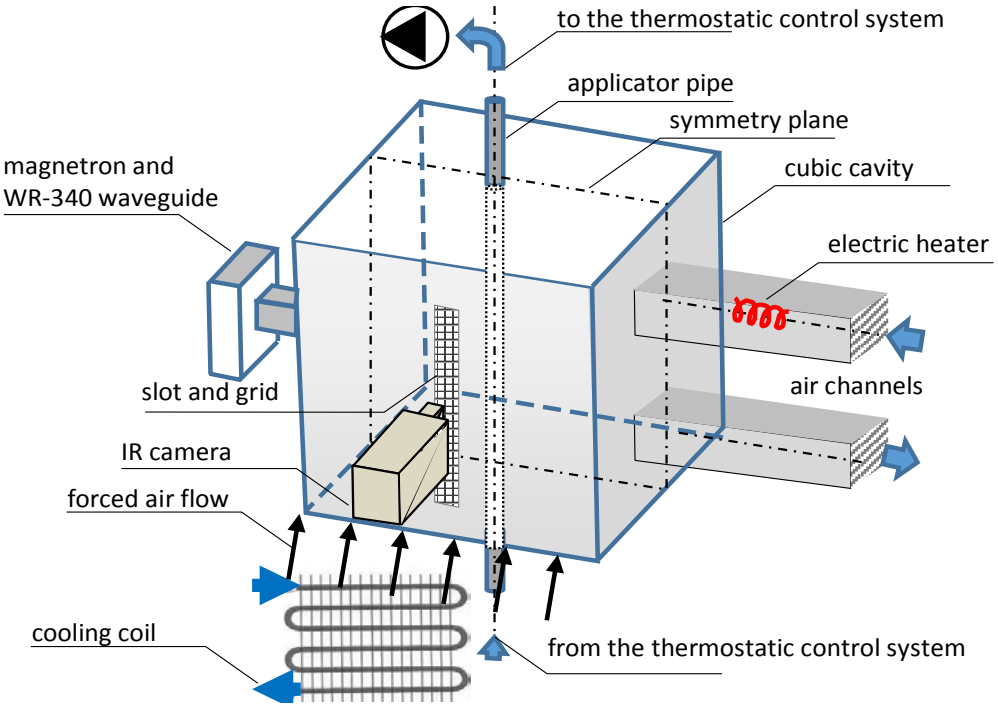

Fig.1. Sketch of the available MW pilot plant

temperature. After leaving the cavity, water was suitably cooled down by a double-pipe heat exchanger and then discharged in the thermostatic bath again thus realizing a closed loop.

A centrifugal fan allowed air renewal into the cavity in order to stabilize the heat transfer between the pipe and the environment. In addition, an helicoidal fan was operated inside the cavity in order to make the heat transfer coefficient between the pipe wall and the surrounding air uniform and independent of temperature levels.

A longwave IR radiometer, thermaCAM by Flir mod. P65, looked at the target pipe through a rectangular window, dim. 30 mm x 700 mm. Such a slot was properly shielded with a metallic grid preventing the EM radiation to leave the cavity whilst resulting almost transparent to the infrared radiation. A cooling system enabled to prevent temperature increase along the grid, probably due to the eddy currents produced by microwaves. In particular, the cooling system consisted of a fan coil placed under the grid. Thus, a cooling air flow was suitably forced pa rallel to the grid, in order to establish its temperature to 19 ± 1.5°C.

B. The numerical procedure

The developing temperature field for an incompressible duct flow subjected to heat generation is considered. A 3D numerical FEM model was developed to predict the EM field distribution in water continuously flowing and the subsequent established temperature field.

The illuminated cavity replied the geometry of one half of the experimental available setup, as previously specified. Such a domain was discretized using unstructured tetrahedral grid elements and taking care in choosing their size. The common sampling criterion due to Nyquist provides the maximum size of the elements to be minor than one half of the wavelength [25]. Some studies (see for instance [5]) suggest that an acceptable criterion is to use six grids per wavelength which could be not always satisfying as reported in [11]. The limit reported above was strictly satisfied for the moving fluid (i.e. $\lambda_{water}/\Delta X_{water} > 30$, λ_{water} being 0.09 m). The same limit is satisfied for the air only where needed around the applicator-pipe. Thus, meshing required 704175 tetrahedral elements, 75288 triangular elements, 3403 edge elements and 76 vertex elements.

Water is described as an isotropic and homogeneous dielectric medium with electromagnetic properties dependent on temperature.

Maxwell's equations were solved in the frequency domain. The electric field distribution $\underline{E}$ in the microwave cavity, both for air and for the applicator pipe carrying the fluid under process, was determined by imposing.

$$\nabla\times\left(\frac{1}{\mu_r}\nabla\times\underline{E}\right)-k_0^2\left(\varepsilon_r-\frac{i\sigma}{\omega\varepsilon_0}\right)\underline{E}=\underline{0} \tag{1}$$

in which ε_r is the relative permittivity, ω is the angular wave frequency, μ_r is the relative permeability of the material, k_0 is the wavenumber in vacuum, and σ is the electric conductivity.

Air and the PTFE applicator tube were both supposed to be completely transparent to microwaves. Boundary conditions included perfect electric conductors walls, that is, $\underline{n}\times\underline{E}=\underline{0}$, for the waveguide and the cavity, $\underline{n}$ being the local normal vector. At the port, an amount of 2kW EM power, 2450MHz frequency, was supplied through a rectangular TE10 mode waveguide (WR 340). Continuity boundary condition was set by default. The condition of perfect magnetic conductor was applied for the surfaces yielding on the symmetry plane: $\underline{n}\times\underline{H}=\underline{0}$, $\underline{H}$ being the magnetic field, which has to be therefore parallel to the local normal vector $\underline{n}$ on the symmetry plane (see Fig. 1).

Temperature distribution is determined for laminar fully developed Newtonian fluid considering constant flow properties; thus, the axial velocity component is given by the parabolic velocity profile. In such hypotheses, the energy balance reduces to

$$\rho c_p U\frac{\partial T}{\partial X}=k\nabla^2 T+U_{gen} \tag{2}$$

where T is the temperature, ρ is the fluid density, c_p is the specific heat, k is the thermal conductivity, X is the axial coordinate, $U(R)$ is the axial Poiseille velocity profile, R the radial coordinate; U_{gen} is the "electromagnetic power loss density" (W/m^3) realizing the coupling with the EM field:

$$U_{gen}(X,Y,Z)=\frac{1}{2}\omega\varepsilon_0\varepsilon''\left|\underline{E}(X,Y,Z)\right|^2 \tag{3}$$

being ε_0 is the free-space permittivity and ε" is the relative dielectric loss of the material. Adiabatic boundary conditions are given both on pipe walls and symmetry plane, while uniform temperature is assumed at inlet. Assuming adiabatic pipe walls stems from considering that heat convection between pipe and air is negligible with respect to the heat generated in the water domain, due to the small interface area. Temperature dependent dielectric properties were considered, approximated by third order polynomials [7].

III. Temperature Readout Procedure

The effect of the grid between the target-pipe and the radiometer has to be accounted to perform wall temperature detection. The focus was set on the applicator pipe and it was checked that the instantaneous field of view of the radiometer in use may well find the hot spots corresponding to the pipe below the grid. Nevertheless, the slit response effect determines the object's temperature to drop as the distance from the radiometer increases. On the other hand, placing the radiometer far from the camera augmented the portion of pipe envisioned. Thus, an acceptable compromise was reached allowing to measure 0.63 m along the pipe axis @ 0.83 m distance from the target. A preliminary calibration and a

suitable procedure have been then adopted. First, the glass-pipe, the grid and the cavity walls have been coated with a high emissivity black paint to reduce reflections. The emissivity value was measured to be ε = 0.95; it was found almost independent of the relative position of the target with respect to the IR camera. Then, two scene-configurations have been considered: the former, i.e. the "test configuration", consists of the applicator-pipe carrying the fluid @ fixed inlet temperature; the latter, i.e. the "reference configuration", provides a polystyrene slab placed inside the cavity in order to hidden the pipe to the radiometer. The shielding slab was black painted too and its temperature, T_{slab}, was measured averaging four fiberoptic probes and pyrometer readouts. In particular the pyrometer sensed over 6 cm^2 area.

For both scenes, neglecting the atmosphere contribution, the fundamental equation of IR thermography relates the spectral radiant power incident on the radiometer to the radiance leaving the surface under consideration. For the case at hand, the attenuation due to the grid must be taken into account. The radiance coming from the inner oven walls is attenuated by a factor τ, here defined as "grid transmittance", which accounts for the SRF grid effect. The latter parameter depends on both the geometry and the temperature level involved. Additionally, the radiometer receives both the radiance reflected from the external surroundings to the grid and the emission by the grid itself. The inner and outer surrounding environments are considered as blackbodies @ uniform temperatures T_i and T_o, respectively. Finally, the radiometric signal weighted over the sensitivity band by the spectral response of the detection system, including the detector sensitivity, the transmissivity of the optical device and amplification by the electronics, is proportional to the target radiance. For the the "reference" and "test" scenes it can be set as follows:

$$I(T_{slab}^{app}) = \tau\,[\varepsilon\, I(T_{slab}) + (1-\varepsilon)\, I(T_i)] + \\ +(1-\tau)\,[\varepsilon\, I(T_{grid}) + (1-\varepsilon)\, I(T_o)] \quad (4)$$

$$I(T_{pipe}^{app}) = \tau\,[\varepsilon\, I(T_{pipe}) + (1-\varepsilon)\, I(T_i)] + \\ +(1-\tau)\,[\varepsilon\, I(T_{grid}) + (1-\varepsilon)\, I(T_o)] \quad (5)$$

here: I is the blackbody Planck's intensity function, evaluated at a suitable wavelength, within the radiometer spectral sensitivity window, λ^+; the apparent temperatures for the pipe, T_{pipe}^{app}, and the polystyrene slab, T_{slab}^{app}, are the surface ones given by an equivalent blackbody as seen by the IR equipment.

With reference to the radiometer in use, λ^+ turns out to be 11.5 μm, as obtained by instrument calibration data.

Inspecting the above equations, the exogen contributions due to both the reflections arising from inner and outer walls clearly appear. Only the former contribution is attenuated by the presence of the grid. The last contribution represents the reinforcement due to the grid emission. The grid transmittance must be considered strongly dependent on the position since the grid contribution to emission assumes a different weight from point to point. In facts, in spite of the tangential air flow running over the grid, an irregular temperature distribution is still observed, probably arising as an after effect of eddy currents occurrence.

Most commonly in thermography, subtracting the two previous equations (4) and (5), the contributions due to both the grid and the inner and outer environments disappear, thus yielding "the net equivalent emissivity for cold surroundings", $\varepsilon\tau$ - function:

$$\varepsilon\tau = \frac{I(T_{pipe}^{app}) - I(T_{slab}^{app})}{I(T_{pipe}) - I(T_{slab})} \quad (6)$$

An image is shown as an example after the subtraction in Fig. 2.

In order to explicit the dependence of the radiance on the temperature, the Plank's law can be rearranged, considering that

$$\frac{dI_{b,\lambda}/I_{b,\lambda}}{dT/T} = \frac{C_2}{\lambda T}\frac{e^{\frac{C_2}{\lambda T}}}{e^{\frac{C_2}{\lambda T}}-1} \approx \frac{C_2}{\lambda T} \quad (7)$$

C_2 = 14390 μm K being the 2nd radiation constant. The approximation due to Wien, which is recalled in the last passage, leads to an error less that 1% if the wavelengths are not greater than 2.5 λ_{max}, λ_{max} being the wavelength for which the maximum emission is attained at the actual temperature. These conditions are fully recovered for the case at hand. In view of the previous expression, if one assumes $I \approx T^n$, it is readily recovered that $n \approx 5\ \lambda_{max} / \lambda^+$. Finally, the last expression can be set as:

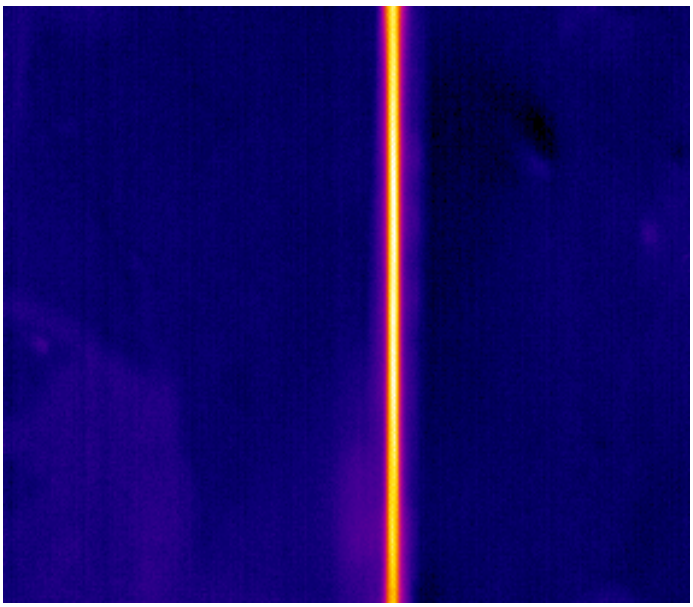

Fig. 2. Net apparent applicator-pipe temperatures

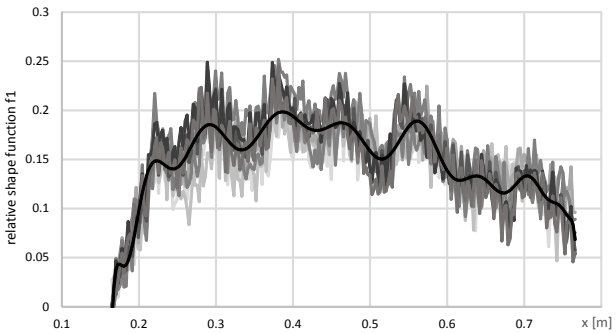

Fig 3. Measured and interpolated relative shape-function f_1

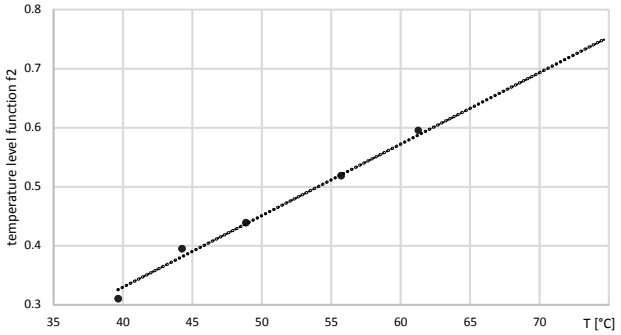

Fig 4. Temperature level function f_2 obtained with a linear regression

$$\varepsilon\tau = \frac{\left(T_{\text{pipe}}^{\text{app}}\right)^{n(T_{\text{pipe}}^{\text{app}})} - \left(T_{\text{slab}}^{\text{app}}\right)^{n(T_{\text{slab}}^{\text{app}})}}{\left(T_{\text{pipe}}\right)^{n(T_{\text{pipe}})} - \left(T_{\text{slab}}\right)^{n(T_{\text{slab}})}} \tag{8}$$

The notation resembles that the index n depends on the temperature itself. In view of this equation, provided the apparent temperatures are known via IR thermography and the slab temperature averaging the fiberoptic probes readout, the function $\varepsilon\tau$ is required in order to infer the pipe temperature. The calibration is then intended to determine $\varepsilon\tau$ as function of both geometry and temperature levels. The calibration is carried on as follows. First, the water flow through the pipe was kept as high as the fluid in the cavity could undergo a linear bulk temperature increase. The overall bulk temperature increase was contained within $\Delta T_{\text{bulk}} = 2.8°C$

Thus, measuring the fluid inlet and outlet temperatures by thermocouples placed externally to the cavity, allowed to know the true bulk temperature along the longitudinal x axis of the pipe, $T_{\text{pipe}}^{\text{bulk}}(x)$ and to fix the corresponding temperature level for the test at hand. Seven inlet temperatures, namely T_{inlet} = 40, 50, 55, 60, 65, 70 and 75 °C, were considered which covered the temperature range involved in the successive experimental tests.

Assuming that the local surface pipe temperature closely approaches the flowing fluid bulk temperature $T_{\text{pipe}}(x) \cong T_{\text{pipe}}^{\text{bulk}}(x)$, knowing the apparent temperatures via IR thermography and measuring the slab temperature, the $\varepsilon\tau$ function can be readily evaluated from eq. (8) for each point along the pipe longitudinal axis (x). The procedure was repeated for the seven preset true temperature levels, simply determined as the average between the inlet and outlet measured values.

Results show that the relative-shape of the $\varepsilon\tau$-function doesn't change with temperature level. Thus, the structure replying the $\varepsilon\tau$-function was sought as $\varepsilon\tau(x, T) = f_1(x) + f_2(T)$. The function f_1 was recovered by averaging the seven relative shapes and turned out to be well approximated (R^2 = 0.994) by a 49-th order polynomial, Fig. 3, while f_2 resulted to be almost linear with temperature, Fig. 4. An average relative error was calculated resulting contained within 2.2%.

The knowledge of the $\varepsilon\tau$–function enables the IR image processing described in the following section.

IV. Image Processing

In view of the discussion previously presented, experiment related to test-scene were performed. After attaining steady state conditions, an image sequence at the rate of 10 images per second was taken for two seconds. Since frames in time sequence differ only in the distribution of random noise, twenty frames were averaged to form a single image with noise variance reduced proportionally to the sequence length. Performing an horizontal scan of the formed image, the maximum apparent temperature for each row was extracted, identifying in such way the pipe apparent temperature along the front-to-radiometer axis.

In a similar fashion, processing an image sequence related to reference scene, the apparent slab temperatures were extracted in correspondence of the previously selected pixels. Finally, eq. (8) was solved for each point to recover the unknown true pipe temperature T_{pipe}, T_{slab} being measured by averaging the fiberoptic probes and pyrometer measurements.

V. Results and Discussion

Two inlet temperature values were considered, namely 40 and 50 °C. For both temperature levels, the average velocity was U_{av} = 0.065 m/s. Each test was replied in triplicate; in particular, Fig. 5 shows the average value of the experimental data and the correspondent local standard deviations, whose maximum resulted to be 3.46 and 3.79 °C for T_{in} = 40 and 50 °C, respectively.

The input power feeding the numerical model was chosen such that the total power heat loss in water was the same of the one resulting from the experiments. The latter was evaluated by calorimetric computations. After that, numerical wall temperatures profiles were extracted, in correspondence of the circumferential coordinate determined by the position of the infrared camera.

Both the numerical and experimental profiles corresponding

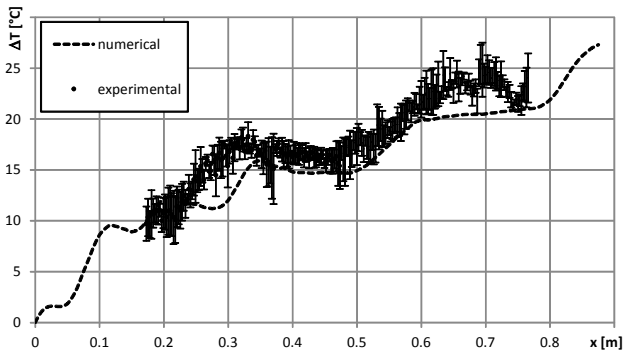

T_{in} = 40 °C and U_{av} = 0.065 m/s

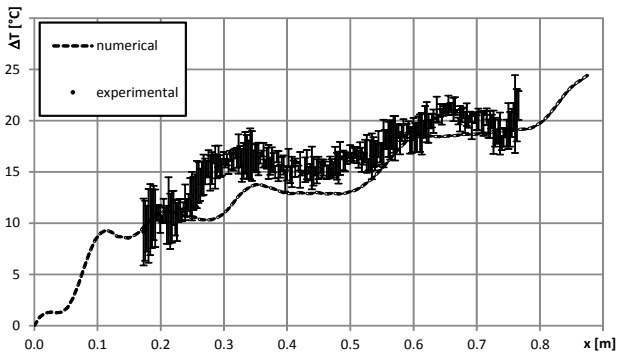

T_{in} = 50 °C and U_{av} = 0.065 m/s

Fig.5. Numerical vs experimental wall temperatures

to the higher inlet temperature are featured by a lower temperature level while keeping almost the same shape. Such a behavior is expected since the higher temperature level exhibits lower absorption rates due to the dependence of the relative dielectric loss of water on temperature. A quite satisfying agreement between experimental and numerical data exists, at least in terms of qualitative behavior: the uneven temperature distribution which is due, in turn, to the EM field patterns, seems to be recovered. Very hardly, such a behavior could be recovered by measuring few temperatures.

VI. Conclusions and Further Work

Wishing to overcome traditional limitations in measuring temperatures inside a MW illuminated cavities, a new experimental procedure based on IR thermography was developed. That enabled to realize high resolution temperature detection. In such a way the wall axial temperature distribution for laminar pipe flow in the developing thermal region was recovered. For both the temperature levels under test, namely 40 and 50 °C, the measured wall temperature profiles were compared with the corresponding results obtained by solving a FEM model, which accounts for dielectric properties temperature dependence. A quite satisfying agreement between experimental and numerical data was found.

Authors are working in order to apply the above procedures to turbulent flow conditions, therefore being able to extend results to wider flow and temperature ranges.

Moreover, electromagnetic adaptation to target will be pursued and energy consumption measured in order to identify, if any, selected pipe collocations inside the cavity.

References

[1] A.C. Metaxas, and R.J. Meridith, *Industrial Microwave Heating*, Peter Peregrinus, London, 1983.

[2] C. Saltiel, and A. Datta, "Heat and mass transfer in microwave processing", *Adv. Heat Transfer*, vol. 30, pp. 1–94, 1997.

[3] X. Jia, and P. Jolly, "Simulation of microwave field and power distribution in a cavity by a three dimensional finite element method", *J Microw Power Electromagn Energy*, vol. 27, no. 1, pp. 11–22, 1992.

[4] R. C. Anantheswaran, and L. Liu, "Effect of viscosity and salt concentration on microwave heating of model non-Newtonian liquid foods in a cylindrical container", *J Microw Power Electromagn Energy*, vol. 29, no. 2, pp. 119–126, 1994.

[5] Q. Zhang, T. H. Jackson, and A. Ungan, "Numerical modeling of microwave induced natural convection", *Int J Heat Mass Transf*, vol. 43, pp. 2141–2154, 2000.

[6] J. Zhu, A. V. Kuznetsov, and K. P. Sandeep, "Numerical simulation of forced convection in a duct subjected to microwave heating", *Heat Mass Transfer*, vol. 43, pp. 255–264, 2007.

[7] G. Cuccurullo, L. Giordano, and G. Viccione, "A fast and accurate hybrid model for simulating continuous pipe flow microwave heating of liquids", *International Journal of Mechanics*, vol. 8; pp. 45-52, 2014.

[8] Q. Zhang, T.H. Jackson, and A. Ungan, "Numerical modeling of microwave induced natural convection", *International Journal of Heat and Mass Transfer*, vol. 43, pp. 2141–2154, 2000.

[9] C.M. Sabliov, D.A. Salvi, and D. Boldor, "High frequency electromagnetism, heat transfer and fluid flow coupling in ANSYS multiphysics", *Journal of Microwave Power & Electromagnetic Energy*, vol. 41, no. 4, pp. 5-17,

[10] P.D. Muley, and D. Boldor, "Multiphysics Numerical Modeling of the Continuous Flow Microwave-Assisted Transesterification Process", *Journal of Microwave Power and Electromagnetic Energy*, vol. 46, no. 3, pp. 139-162, 2012.

[11] G. Cuccurullo, L. Giordano, and G. Viccione, "An analytical approximation for continuous flow microwave heating of liquids", *Advances in Mechanical Engineering*, vol. 2013, Article ID 929236, 8 pages, 2013.

[12] G. Cuccurullo, L. Giordano, and G. Viccione, "Toward an Improved Hybrid Model for Simulating Continuous Flow Microwave Heating of Water", In: *Recent Advances in Mechanics, Fluids, Heat, Elasticity and Electromagnetic Fields*, Venezia, 2013, pp.182-189.

[13] D. Salvi, D. Boldor, J. Ortego, G.M. Aita, and C.M. Sabliov, "Numerical Modeling of Continuous Flow Microwave Heating: A Critical Comparison of COMSOL and ANSYS", *Journal of Microwave Power and Electromagnetic Energy*, vol. 44, no. 4, pp. 187-197.

[14] M. De Pourcq, "Field and power density calculation in closed microwave system by three-dimensional finite difference", In: *IEEE Proc*, vol. 132, no. 11, 1985, pp. 361–368.

[15] J.P. Webb, G.L. Maile, and R.L. Ferrari, "Finite element implementation of three dimensional electromagnetic problems", In: *IEEE Proc*, vol. 78, 1983, pp. 196–200.

[16] S.V. Patankar, *Numerical heat transfer and fluid flow*, Hemisphere, New York, 1980.

[17] K.G. Ayappa, H.T. Davis, E.A. Davis, and J. Gordon, "Two-dimensional finite element analysis of microwave heating", *AIChE J*, vol. 38, pp. 1577–1592, 1992.

[18] P. Ratanadecho, K. Aoki, and M. Akahori, "A numerical and experimental investigation of the modeling of microwave heating for liquid layers using a rectangular wave guide (effects of natural convection and dielectric properties)", *Applied Mathematical Modelling*, vol. 26, no. 3, pp. 449–472, 2002.

[19] G. Cuccurullo, L. Giordano, and G. Viccione, "Looking inside a microwave oven for continuous flow heating by IR Thermography", In: *Proceedings of the 10th WSEAS International Conference on Applied and Theoretical Mechanics (MECHANICS '14)*, Salerno, 2014, pp. 47-54.

[20] H. Zhao, and I.W. Turner, "An analysis of the finite-difference time-domain method for modeling the microwave heating of dielectric materials within a three-dimensional cavity system", *J Microw Power Electromagn Energy*, vol. 31, no. 4, pp. 199–214, 1996.

[21] G. Cuccurullo, L. Giordano, D. Albanese, L. Cinquanta, and M. Di Matteo, "Infrared thermography assisted control for apples microwave drying", *Journal of Food Engineering*, vol. 112, no. 4, pp. 319 – 325, 2012.

[22] T. M. Finegan, *Remote three-dimensional temperature sensing using planar laser induced fluorescence: development and applications to microwave heated liquids*, Ph.D. thesis, Massachusetts Institute of Technology. Dept. of Chemical Engineering, 2004.

[23] Nai-Yu Wang, and J.F. Vesecky, "Sea surface temperature estimation using active/passive microwave remote sensing", In: *Geoscience and Remote Sensing Symposium, IGARSS '99 Proceedings*. 1999, vol. 2.

[24] G. Viccione, and V. Tibullo, "An effective approach for designing circular pipes with the Colebrook-White formula", In: *International Conference of Numerical Analysis and Applied Mathematics (ICNAAM)*, Kos (Greece), 19–25 September 2012, vol.1479, 2012, pp. 205-208.

[25] C. Mirabito, A. Narayanan, D. Perez, and B. Stone, "FEMLAB model of a coupled electromagnetic–thermal boundary value problem". Research Experience: Worcester Polytechnic Institute, MA, 2005.